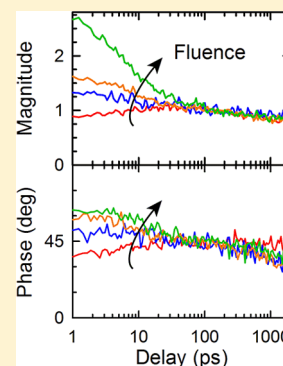# Multiple Population-Period Transient Spectroscopy (MUPPETS) of CdSe/ZnS Nanoparticles. II. Effects of High Fluence and Solvent Heating

Haorui Wu, Kalyanasis Sahu,[†] and Mark A. Berg*

Department of Chemistry and Biochemistry, University of South Carolina, Columbia, South Carolina 29208, United States

S *Supporting Information*

ABSTRACT: Multiple population-period transient spectroscopy (MUPPETS) is a six-pulse experiment with two time dimensions that is capable of adding information about systems with complicated kinetics. The core theory for MUPPETS focuses on the $\chi^{(5)}$ response of the chromophores. This theory was used to analyze the dynamics of excitons and biexcitons in CdSe/ZnS core–shell nanoparticles in part I of this paper [*J. Phys. Chem. B* **2013**, DOI:10.1021/jp405785a]. In real experiments, the potential role of additional processes must also be considered, in particular, the $\chi^{(7)}$, "saturation" of the MUPPETS signal and nonresonant signals from heating of the solvent. A pathway method for calculating fluence effects in MUPPETS is developed. The fluence dependence of the biexciton signal and its sign reversal, as found in part I, are explained without invoking higher excitons or unexpected species. A method is presented for quantitatively predicting the magnitude of signals from solvent heating using an external standard. Thermal effects in this system are found to be too small to affect the conclusions in part I. Their small size, combined with small, systematic errors in the data, also makes it difficult to measure the yield of solvent heat in these experiments.

1. INTRODUCTION

In part I of this paper,[1] the dynamics of excitons and biexcitons in CdSe/ZnS core–shell nanoparticles were analyzed with multiple population-period transient spectroscopy (MUPPETS). MUPPETS is a form of two-dimensional (2D) kinetics, i.e., it contains two variable time intervals. In systems with complicated kinetics, MUPPETS provides information about the heterogeneity of the system and the connections between the relaxation of different transitions. MUPPETS is a six-pulse experiment, and as a result, the core theory for MUPPETS focuses on the $\chi^{(5)}$ response of the chromophores.[2−5] This theory was used in part I. However, in real experiments, other processes must be considered, in particular, higher order responses of the chromophores and the thermal response of the solvent. This part of the paper presents new methods for analyzing these secondary effects and applies them to the data presented in part I.

Part I confirmed the prediction that the MUPPETS signal has a negative biexciton component in the low-fluence limit. However, this feature was rapidly lost with modest fluence increases and was replaced with a similar positive feature. One concern is that another, unexpected species is involved, such as a photoproduct or higher exciton, with unforeseen effects on the nominally low fluence data.

This problem is addressed by extending the calculation of the signal to include $\chi^{(7)}$ "saturation" terms. We show how the Hilbert-space pathway formalism[2,3] for calculating MUPPETS can be extended to include these processes. The calculation readily explains all the observed fluence effects. Concerns about unknown species are alleviated, and the conditions needed to avoid saturation are quantified.

Solvent thermal effects in MUPPETS are an extension of the thermal gratings and thermal lenses seen in lower order experiments.[6−9] The relaxation of the excited state of a solute typically heats the surrounding solvent. The resulting change in index-of-refraction of the solvent can be detected optically by diffraction or deflection of the probe beam. The size of this signal from the solvent is often similar to the change in solute absorption. We have observed strong thermal effects in MUPPETS experiments in other systems.[10] Detailed theory and experimental data showing thermal effects in MUPPETS with two-level chromophores have been reported before,[10,11] and the basic theory for thermal effects in excitonic systems has been presented recently.[5] In general, thermal effects present a hazard if they are not correctly separated from the resonant signals.

On the other hand, in one-dimensional (1D) experiments, thermal effects have been useful in measuring the heat released in chemical processes, which is otherwise spectroscopically unobservable.[12−16] In a similar manner, thermal effects in MUPPETS might yield information on trap states—long-lived, optically dark states that do not release heat to the solvent. In

CdSe nanoparticles, such traps are sometimes invoked as the final state for exciton and biexciton relaxation.

A particular example is the biexciton signal measured in part I of this paper (Figure I.9B).[1] It shows an unexplained signal recurrence at long times that is qualitatively consistent with a thermal effect. Does this signal isolate the biexciton thermal effect as it isolates the biexciton resonant effect? Does the size of the signal provide a measure of the yield of trap states?

Answering these questions requires an independent calibration of the expected size of the thermal effects. We will show that it is possible to use an external standard to determine the ratio of thermal to resonant signal sizes. The calibration shows that the thermal effects should be small in this system and do not affect the conclusions of part I. Unfortunately, their small size also makes them comparable to systematic errors in the data. In the experiments, it is difficult to draw firm conclusions about the yield of trap states.

In general, the additional analysis in this part of the paper will not change any of the conclusions about the dynamics of excitons or biexcitons drawn in part I. However, it provides the theory for secondary processes in MUPPETS experiments and a practical example of how to control for them.

2. FLUENCE-INDUCED SIGNALS

We introduced a Hilbert-space pathway method for treating incoherent experiments with N time dimensions, including 2D-MUPPETS experiments.[2−5] This method has been used previously only to calculate the low-fluence limit of these experiments. This section shows how this approach can be extended to include the first-order fluence dependence, both in the case of a general N-dimensional experiment and in the specific case of 2D-MUPPETS on an excitonic system. Section 2.1 summarizes the method and notation in the low-fluence case. Section 2.2 introduces fluence-induced calculations and illustrates their use in the more familiar case of 1D measurements. New results for 2D-MUPPETS are produced in section 2.3. They are then compared to the experimental data of part I in section 2.4.

2.1. Standard Pathway Method. The method associates every incoherent state (quantum-mechanical population state) with a vector $|P]$ in a Hilbert-space. (The analogy with quantum Hilbert-space vectors $|\psi\rangle$ is intentional and well-defined.[2]) The signal is calculated as the generalized, complex absorbance of the $(N+1)$th pulse-pair $A^{(N)}$ (eq I.1). It is found by taking the product of the detection cross-section vector $[\sigma_D|$ with the final-state vector $|f^{(N)}]$

$$A^{(N)} = (-1)^N \rho L [\sigma_D | f^{(N)}] \tag{1}$$

The density of chromophores is ρ, and the length of the sample is L. Because the states represent the entire sample, not a single molecule, an ensemble average is implied by the vector product.

The final state is created from the initial, equilibrium state $|eq]$ by N optical transitions alternating with periods of free time evolution. In MUPPETS, each excitation is created by a pair of pulses, each pulse contributing one electric-field interaction. The nth optical excitation at time t_n is represented by the transition operator $\mathbf{T}_n$, and the evolution between transitions is represented by the operator $\mathbf{G}(t_{n+1}, t_n)$. The operator $\mathbf{G}(t_{n+1}, t_n)$ refers to the dynamics of a single chromophore. For nonexponential decays, it depends on the time from the first excitation t_n, as well as the time interval, $\tau_n = t_n - t_{n-1}$. Thus, the signal is calculated from

$$A^{(N)}(\tau_N, ..., \tau_1) = (-1)^N \rho L [\sigma_D | \mathbf{G}(t_N, t_{N-1}) \mathbf{T}_N$$
$$\times ... \mathbf{G}(t_1, t_0) \mathbf{T}_1 | eq] \tag{2}$$

In a system without significant polarization effects, and in an experiment in which only one pulse combination is well phase-matched, the transition operator $\mathbf{T}_n$ is a simple product of I_n, the geometric-mean fluence of the nth pulse-pair, and the optical transition cross-section operator σ_T

$$\mathbf{T}_n = I_n \sigma_T \tag{3}$$

For simplicity, all the excitation pulses will be assumed to have the same fluence. Both the transition cross-section operator σ_T and the detection cross-section vector $[\sigma_D|$ are constructed from a model of the system's spectroscopy (e.g., Figure I.7A), but the two are not identical.

Pathways are generated by selecting a basis set and using it to enumerate all possible intermediate states in eq 2. Our model of the electronic states of CdSe nanoparticles (Figure I.7A) defines three states: the ground state $|0]$, the exciton $|1]$, and the biexciton $|2]$. (The fast relaxing fine structure within the exciton and biexciton states are incorporated into an effective optical-transition cross-section operator σ_T for the system.[3]) The number of pathways in the calculation can be minimize by switching to a basis set with strong selection rules on σ_T and $\mathbf{G}$. For an excitonic system, the best basis set is nonorthogonal: $|0'] = |0]$, $|1'] = (|1]-|0])/\sqrt{2}$ and $|2'] = (|2]-|1])/\sqrt{2}$.[5]

The notation is more compact if the matrix elements of an operator $\mathbf{O}$ are written

$$O_j^i = [j|\mathbf{O}|i] \tag{4}$$

and those of a vector $|P]$ are written

$$P_i = [i|P] \tag{5}$$

or

$$P^i = [P|i] \tag{6}$$

(Because a nonorthogonal basis set is used, bras and superscripts are not equivalent to kets and subscripts.[17]) Starting with eq 3 and inserting complete sets of states between all the operators in eq 2 yields

$$A^{(N)}(\tau_N, ..., \tau_1) = (-1)^N \rho L I^N (\sigma_D)^n G_n^m(t_N, t_{N-1})(\sigma_T)_m^l$$
$$\times ... G_j^i(t_1, t_0)(\sigma_T)_i^{eq} \tag{7}$$

The convention of summation over repeated indices is used.[17] Each term in the implied sum is one pathway.

Collecting all the time-evolution terms and averaging them over the ensemble creates an N-dimensional correlation function

$$C_{n,...,j}^{m,...,i}(\tau_N, ..., \tau_1) = G_n^m(t_N, t_{N-1})...G_j^i(t_1, t_0) \tag{8}$$

Equation 7 becomes

$$\frac{A^{(N)}(\tau_N, ..., \tau_1)}{A'^{(0)}} = (-1)^N I^N [(\sigma_D)^n (\sigma_T)_m^l ... (\sigma_T)_k^j]$$
$$\times C_{n,...,j}^{m,...,1'}(\tau_N, ..., \tau_1) \tag{9}$$

where the static absorbance of the sample is $A'^{(0)} = \rho L (\sigma_T)_{1'}^{0'}$. We have used the facts that at equilibrium, all the molecules are in the ground state, $|0'] = |eq]$, and that the first intermediate

state i is always $|1'|$ when the exciton basis set is used.[5] Each pathway in eq 9 consists of a correlation function and a weight represented by the term in square brackets.

The application of this general formalism to the specific cases of 1D and 2D experiments, $A^{(1)}(\tau_1)$ and $A^{(2)}(\tau_2, \tau_1)$ respectively, in the CdSe system is illustrated in Figures 1
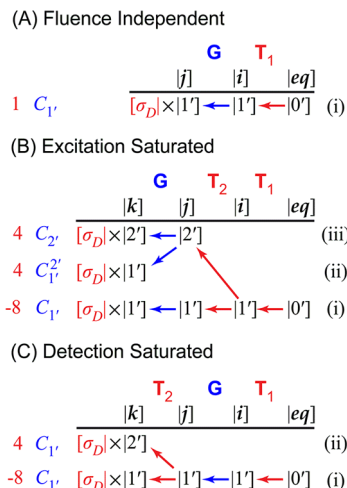

Figure 1. Pathways used to calculate the resonant signal in 1D (pump−probe and transient-grating) experiments, including the fluence dependence. The population states $|P|$ are transformed by a sequence of optical transitions (red), which are governed by the operator $\mathbf{T}$, and free evolution in time (blue), which is governed by the operator $\mathbf{G}$. The final state is measured by taking the product of the final state with the detection vector $[\sigma_D|$. On the far left, each pathway is labeled with its relative weight, which is determined by the product of transition and detection matrix elements (red). The relative weights are shown here for the simple case $\sigma_{01} = \sigma_{12} = 1$. On the near left, each pathway is labeled by its correlation function C_x, which is determined by the product of time-evolution matrix elements (blue). (A) Pathways with no fluence dependence. (B) Pathways with fluence dependence due to two interactions with the excitation pulses. (C) Pathways with fluence dependence due to two interactions with the detection pulses.

and 2. The low-fluence contributions, $A_A^{(1)}(\tau_1)$ and $A_A^{(2)}(\tau_2, \tau_1)$, are due to the pathways in Figures 1A and 2A. The relevant sequence of operators from the expressions

$$A_A^{(1)}(\tau_1) = -\rho L[\sigma_D|\mathbf{G}(t_1, t_0)\mathbf{T}_l|0']$$ (10)

and

$$A_A^{(2)}(\tau_2, \tau_1) = \rho L[\sigma_D|\mathbf{G}(t_2, t_1)\mathbf{T}_2\mathbf{G}(t_1, t_0)\mathbf{T}_l|0']$$ (11)

(cf. eq 2) are given on the top of each panel. Immediately below are labels for the intermediate states used to define the pathways in the expressions

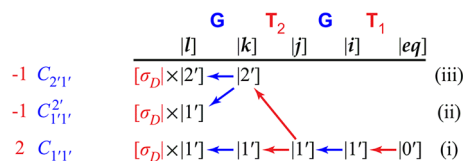$$\frac{A_A^{(1)}(\tau_1)}{A'^{(0)}} = -I(\sigma_D)^j C_j^{1'}(\tau_1)$$ (12)

and

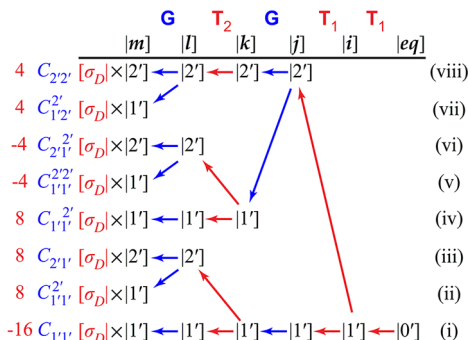$$\frac{A_A^{(2)}(\tau_2, \tau_1)}{A'^{(0)}} = I^2(\sigma_D)^l(\sigma_T)_k^j C_{l,j}^{k,1'}(\tau_2, \tau_1)$$ (13)

(cf. eq 9).

Nonzero pathways contributing to these sums are listed below the solid lines. The basis set has been chosen to impose
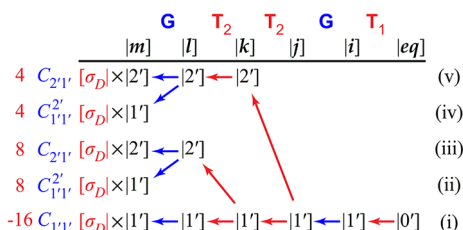
Figure 2. Pathways used to calculate the resonant signal in 2D (MUPPETS) experiments, including the fluence dependence. The format is explained in the caption to Figure 1. (A) Pathways with no fluence dependence. (B) Pathways with fluence dependence due to saturation of the excitation pulses. (C) Pathways with fluence dependence due to saturation of the detection pulses.

strong selection rules to limit the number of pathways.[5] The only allowed transition out of the initial state $|0'|$ is to $|1'|$, and its cross-section is included in $A'^{(0)}$. Subsequent transitions in the CdSe system are governed by[5]

$$(\sigma_T)_j^i = \begin{pmatrix} -\sigma'_{12} & \sigma'_{12} \\ 0 & -2\sigma'_{01} \end{pmatrix}$$ (14)

The initial state $|0'|$ never appears as an intermediate state. As a result, eq 14 (and eq 15 below) are written in the reduced basis set $\{|1'|, |2'|\}$. Time-evolution never takes a state to one with a higher index. For 1D measurements, these restrictions leave only one pathway (Figure 1A). In 2D measurements, they leave three pathways (Figure 2A), which are described more loosely by the ladder diagrams in Figure I.2.

The correlation function for each pathway is constructed from the time-evolution steps of each pathway (eq 8). These are given on the left-hand sides of Figures 1 and 2. The weight for each pathway (bracketed term in eq 9) is given on the far left of Figures 1 and 2. Their calculation requires the detection cross-section vector for the CdSe system,[5]

$$(\sigma_D)^i = -(\sigma_{12} \quad \sigma_e)$$ (15)

with

$$\sigma_e = 2\sigma_{01} - \sigma_{12}$$ (16)

The figures give only the simple case of $\sigma_{01} = \sigma_{12} = \sigma$. The full expressions without this simplification are

$$\frac{A_A^{(1)}(\tau_1)}{A'^{(0)}} = I\sigma_e C_{1'}(\tau_1) \tag{17}$$

and

$$\frac{A_A^{(2)}(\tau_2, \tau_1)}{A'^{(0)}} = I^2[\sigma_e(2\sigma'_{01})C_{1'1'}(\tau_2, \tau_1) - \sigma_e\sigma'_{12}C_{1'1'}^{2'}(\tau_2, \tau_1)$$
$$- \sigma_{12}\sigma'_{12}C_{2'1'}(\tau_2, \tau_1)] \tag{18}$$

For simplicity, a repeated subscript and superscript on a correlation function are only written once, e.g., $C_{1'}^{1'} = C_{1'}$. After normalization (eqs I.2 and I.3) and rewriting the complex cross sections in terms of practical fitting parameters, these equations give the expressions for the low-fluence, 1D and 2D absorbances used in part I (eqs I.10 and I.20, respectively).[1]

2.2. Calculating 1D Fluence-Induced Signals.

The extension of the pathway calculations to fluence-induced signals is illustrated for 1D experiments in Figure 1B. Two interactions occur with the excitation pulse pair, giving the additional absorbance

$$A_B^{(1)}(\tau_1) = -\rho L[\sigma_D|\mathbf{G}(\tau_1, 0)\mathbf{T}_I\mathbf{T}_I|0'] \tag{19}$$

(cf. eq 10). The double interaction is treated as a sequence of incoherent transitions. This approach is appropriate when the excitation pulses are substantially longer than the dephasing time of the transition. In this case, pathways with a population state as an intermediate dominate. For very short excitation pulses, a single operator including two-quantum coherences would need to be derived from first principles.[3]

Expanding into pathways over intermediate states gives

$$\frac{A_B^{(1)}(\tau_1)}{A'^{(0)}} = -\varepsilon_2 I^2(\sigma_D)^k(\sigma_T)_j^{1'}C_k^j(\tau_1) \tag{20}$$

(cf. eq 12). The allowed pathways in this sum are enumerated in Figure 1B, as are the corresponding correlation functions.

The term ε_2 is included in eq 20 to account for the degeneracy in the phase-matching conditions associated with a double interaction. The phase-matching condition for the low-fluence term is

$$(\vec{k}_{1a} - \vec{k}_{1b}) + (\vec{k}_{2a} - \vec{k}_{2b}) = 0 \tag{21}$$

where $\vec{k}_{xy}$ is the k-vector for pulse $y \in \{a, b\}$ of the xth pulse-pair. By assumption, the experiment is designed to allow one and only one phase-matched combination of pulses. The double degeneracy from multiplying this equation by minus one is already included in the definition of the cross-section. Thus there is no degeneracy for the low-fluence experiment.

However, the phase-matching condition for the pathways in Figure 1B is

$$(\vec{k}_{1a} - \vec{k}_{1b}) + (\vec{k}_{1a} - \vec{k}_{1a}) + (\vec{k}_{2a} - \vec{k}_{2b}) = 0 \tag{22}$$

There is a 2-fold degeneracy from swapping the first and second terms in parentheses and another 2-fold degeneracy from transforming a to b in the second set of parentheses. Thus, the total degeneracy for a double interaction of $\mathbf{T}$ is $\varepsilon_2 = 4$. This degeneracy is included in the pathway weights listed in Figures 1 and 2.

Using the cross sections from our system (eqs 14 and 15) in eq 20 gives the total absorbance due to a double interaction with the excitation pulse,

$$\frac{A_B^{(1)}(\tau_1)}{A'^{(0)}} = -4I^2[\sigma_e(2\sigma'_{01})C_{1'}(\tau_1) - \sigma_e\sigma'_{12}C_{1'}^{2'}(\tau_1)$$
$$- \sigma_{12}\sigma'_{12}C_{2'}(\tau_1)] \tag{23}$$

The effects are as expected. The first term represents saturation of the ground-to-exciton transition. The third term is due to the creation of biexcitons. The second term is the cross-relaxation term needed to correct the decay of excitons derived from biexcitons relative to the decay of directly created excitons.

We also consider a double interaction with the probe pulse-pair in Figure 1C. An optical transition between states $\mathbf{T}_2$ occurs immediately before the detection of the final state, giving a contribution to the absorption of

$$A_C^{(1)}(\tau_1) = -\rho L[\sigma_D|\mathbf{T}_2\mathbf{G}(\tau_1, 0)\mathbf{T}_I|\text{eq}] \tag{24}$$

(cf. eq 10). When this equation is expanded into pathways, the general expression is

$$\frac{A_C^{(1)}(\tau_1)}{A'^{(0)}} = -\varepsilon_2 I^2(\sigma_D)^k(\sigma_T)_k^j C_j^{1'}(\tau_2, \tau_1) \tag{25}$$

There are only two nonzero pathways, as shown in Figure 1C. For the CdSe system (eqs 14 and 15), these pathways give

$$\frac{A_C^{(1)}(\tau_1)}{A'^{(0)}} = -4I^2[\sigma_e(2\sigma'_{01}) - \sigma_{12}\sigma'_{12}]C_{1'}(\tau_1) \tag{26}$$

(cf. eq 12). Biexcitons are created too late to contribute to the dynamics; they only alter the effective cross-section of the exciton dynamics. The net effect is to suppress the signal from the excitons.

In many 1D experiments, the probe fluence is attenuated relative to the excitation fluence. Equations 23 and 26 show that the saturation effects of the probe and excitation are quite similar in size. If the excitation is attenuated sufficiently to avoid fluence effects, there is no fundamental need to attenuate the probe further than the excitation. In our 1D experiments, the excitation and probe had the same fluences.

Part I of the paper normalized data at different fluences and extracted low-fluence and fluence-induced components, $A_0^{(1)}(\tau_1)$ and $A_1^{(1)}(\tau_1)$, respectively. To calculate these quantities, all sources of signal, $A_A^{(1)}(\tau_1)$, $A_B^{(1)}(\tau_1)$, and $A_C^{(1)}(\tau_1)$, must be added, and the result normalized according to eq I.2 to give $\bar{A}^{(1)}(\tau_1)$. This quantity is truncated to first order in I and then divided into low-fluence and fluence-induced components:

$$\bar{A}^{(1)}(\tau_1) = A_0^{(1)}(\tau_1) + 4I\sigma'_{12}\frac{|\sigma_{12}|}{|\sigma_e|}A_1^{(1)}(\tau_1) \tag{27}$$

The low-fluence component $A_0^{(1)}(\tau_1)$ is simply related to $A_A^{(1)}(\tau_1)$, giving eq I.10. The result is the same as a calculation without fluence-induced terms. All the terms containing the exciton decay are removed by the normalization, leaving the fluence-induced component

$$A_1^{(1)}(\tau_1) = e^{i\Phi_{12}}\left(C_{2'}(\tau_1) + \frac{\sigma_e}{\sigma_{12}}C_{1'}^{2'}(\tau_1)\right) \tag{28}$$

with only biexciton decay $C_{2'}(\tau_1)$ and cross-relaxation $C_{1'}^{2'}(\tau_1)$ terms. Rewriting the cross sections in terms of practical

parameters gives eq I.11. Although the phenomena involved in the fluence-induced 1D experiments are familiar, we are not aware of a previous derivation that includes the complex cross sections and phase effects needed to describe a heterodyned experiment.

2.3. Calculating 2D Fluence-Induced Signals. The fluence-dependence of the MUPPETS signal is calculated using the same approach used in section 2.2. There are three places where an extra interaction can create additional absorbances: during the first excitation,

$$A_B^{(2)}(\tau_2, \tau_1) = \rho L[\sigma_D | \mathbf{G}(t_2, t_1) \mathbf{T}_2 \mathbf{G}(t_1, t_0) \mathbf{T}_1 \mathbf{T}_1 | 0'] \quad (29)$$

during the second excitation,

$$A_C^{(2)}(\tau_2, \tau_1) = \rho L[\sigma_D | \mathbf{G}(t_2, t_1) \mathbf{T}_2 \mathbf{T}_2 \mathbf{G}(t_1, t_0) \mathbf{T}_1 | 0'] \quad (30)$$

or during the detection

$$A_D^{(2)}(\tau_2, \tau_1) = \rho L[\sigma_D | \mathbf{T}_3 \mathbf{G}(t_2, t_1) \mathbf{T}_2 \mathbf{G}(t_1, t_0) \mathbf{T}_1 | 0'] \quad (31)$$

(cf. eq 11). In our MUPPETS experiments, the probe pulse was attenuated by a factor of 10, primarily to simplify the current calculations by making $A_D^{(2)}(\tau_2, \tau_1)$ small. Thus, we will drop $A_D^{(2)}(\tau_2, \tau_1)$ for the remainder of the paper, although it can be treated with similar methods.

When the other two processes are expanded in pathways, we get

$$\frac{A_B^{(2)}(\tau_2, \tau_1)}{A'^{(0)}} = \varepsilon_2 I^3 (\sigma_D)^m (\sigma_T)_l^k (\sigma_T)_j^{1'} C_{m,k}^{l,j}(\tau_2, \tau_1) \quad (32)$$

and

$$\frac{A_C^{(2)}(\tau_2, \tau_1)}{A'^{(0)}} = \varepsilon_2 I^3 (\sigma_D)^m (\sigma_T)_l^k (\sigma_T)_k^j C_{m,j}^{l,1'}(\tau_2, \tau_1) \quad (33)$$

(cf. eq 13). The allowed pathways are illustrated in Figure 2B–C. The k-vector degeneracies are still those for pairs of interactions, i.e., $\varepsilon_2 = 4$.

The full results are quite complicated, with eight pathways for $A_B^{(2)}(\tau_2, \tau_1)$ and five for $A_C^{(2)}(\tau_2, \tau_1)$. However, part I of the paper has already shown that cross-relaxation in our system is negligibly small. Thus, we drop all pathways whose correlation function contains a $G_{1'}^{2'}$ term. Only three pathways remain for $A_B^{(2)}(\tau_2, \tau_1)$ (i, iii and viii) and for $A_C^{(2)}(\tau_2, \tau_1)$ (i, iii and v). They evaluate to

$$\frac{A_B^{(2)}(\tau_2, \tau_1)}{A'^{(0)}} = -4I^3[\sigma_e (2\sigma'_{01})^2 C_{1'1}(\tau_2, \tau_1)$$
$$- \sigma_{12} \sigma'_{12} (2\sigma'_{01}) C_{2'1}(\tau_2, \tau_1)$$
$$- \sigma_{12} (\sigma'_{12})^2 C_{2'2}(\tau_2, \tau_1)] \quad (34)$$

and

$$\frac{A_C^{(2)}(\tau_2, \tau_1)}{A'^{(0)}} = -4I^3[\sigma_e (2\sigma'_{01})^2 C_{1'1}(\tau_2, \tau_1)$$
$$- \sigma_{12} \sigma'_{12} (2\sigma'_{01}) C_{2'1}(\tau_2, \tau_1)$$
$$- \sigma_{12} (\sigma'_{12})^2 C_{2'1'}(\tau_2, \tau_1)] \quad (35)$$

The first pair of terms in eqs 34 and 35 are the same. They have the same shape as the low-fluence signal (eq 18 with cross-relaxation neglected), but the opposite sign. These terms represent simple saturation of the signal size without a change

in shape. The last terms of both eqs 34 and 35 are due to the creation of extra biexcitons at high fluence. In particular, eq 34 contains a biexciton–biexciton correlation function $C_{2'2'}(\tau_2, \tau_1)$ that has not appear previously.

For comparison to the experimental data, $A_A^{(2)}(\tau_2, \tau_1)$, $A_B^{(2)}(\tau_2, \tau_1)$, and $A_C^{(2)}(\tau_2, \tau_1)$ (eqs 18, 34, and 35) are summed and normalized to the exciton–exciton decay (eq I.3) to give $\bar{A}^{(2)}(\tau_2, \tau_1)$. This expression is expanded in powers of I and truncated at first order to give

$$\bar{A}^{(2)}(\tau_2, \tau_1) = A_0^{(2)}(\tau_2, \tau_1) + 4I\sigma'_{12} \frac{|\sigma_{12}| \sigma'_{12}}{|\sigma_e| \sigma'_{01}} A_1^{(2)}(\tau_2, \tau_1) \quad (36)$$

The expression for the low-fluence component $A_0^{(2)}(\tau_2, \tau_1)$ has already been used to analyze data in part I (eq I.20) and is no different than if the fluence dependent terms had been neglected from the start. The normalization removes all the simple, size-reducing contributions to the fluence-induced component $A_1^{(2)}(\tau_2, \tau_1)$ and leaves only the last, shape-changing terms in eqs 34 and 35:

$$A_1^{(2)}(\tau_2, \tau_1) = \frac{1}{2} e^{i\Phi_{12}} (C_{2'2'}(\tau_2, \tau_1) + C_{2'1'}(\tau_2, \tau_1)) \quad (37)$$

2.4. Analyzing 2D Fluence-Induced Data. The MUPPETS data has a strong fluence dependence that changes the early, rising signal into a decay (Figure I.8A–B). This behavior can now be explained. Focusing on the $\tau_1 = 0$ cut through the data is sufficient. Neglecting cross-relaxation and thermal effects and using our current notation, the $\tau_1 = 0$ low-fluence data should fit

$$A_0^{(2)}(\tau_2, 0) = e^{i\Phi_e} C_{1'}(\tau_2) - \frac{1}{2} \frac{|\sigma_{12}| \sigma'_{12}}{|\sigma_e| \sigma'_{01}} e^{i\Phi_{12}} C_{2'}(\tau_2) \quad (38)$$

(cf. eq I.12). The initial rise in the signal is due to the decay of the negative biexciton signal. The same cut of the fluence-induced data has now been predicted to be (eq 37)

$$A_1^{(2)}(\tau_2, 0) = e^{i\Phi_{12}} C_{2'}(\tau_2) \quad (39)$$

Comparing eqs 38 and 39, as the fluence is increased, the negative biexciton signal will be reduced, canceled, and eventually replaced by a positive biexciton contribution. This is exactly the pattern seen in Figure I.8A–B, and these equations fit the data well using the parameters already determined in part I. Thus, the qualitative behavior of the MUPPETS at high fluence is explained.

On a quantitative basis, the fluence-induced MUPPETS signal (eq 39) is predicted to be exactly the same as the fluence-induced 1D signal (eq I.11, neglecting cross-relaxation and thermal effects):

$$A_1^{(2)}(\tau_2, 0) = A_1^{(1)}(\tau_2) \quad (40)$$

The comparison between MUPPETS and transient-grating data is shown in Figure 3. The two signals are identical, as predicted. No new information is gained, but the agreement indicates that no unanticipated states, species or phenomena are accessed in the MUPPETS experiments under the current experimental conditions, even at the highest fluences.

Huxter and Scholes reported biexciton lifetimes of CdSe nanoparticles using a high-order grating technique.[18] Their technique is similar to MUPPETS with τ_1 fixed to zero, and they also used band-edge excitation to avoid creating triexcitons. They did not specifically comment on the fluence

15276

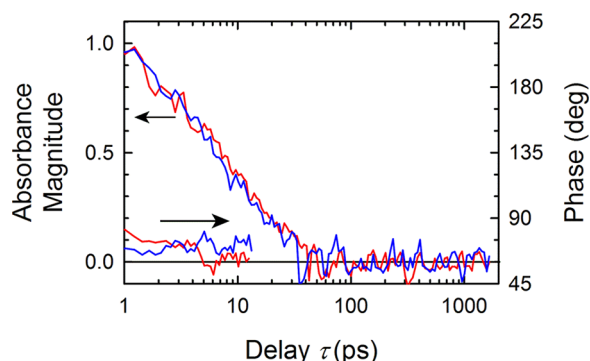dx.doi.org/10.1021/jp4057913 | J. Phys. Chem. B 2013, 117, 15272–15284

Figure 3. Fluence-induced component of the MUPPETS data at $\tau_1 = 0$, $A_1^{(2)}(\tau,0)$ (blue, from Figure I.8C−D) compared to the fluence-induced transient-grating data $A_1^{(1)}(\tau)$ (red, from Figure I.5C−D). Both experiments are predicted to give the biexciton decay $C_{2'}(\tau)$ and are in good agreement.

Figure 4. Fluence-induced component of the MUPPETS data at various values of τ_1. These data are governed by biexciton dynamics. (A) Magnitude of $A_1^{(2)}(\tau_2,\tau_1)$. (The phases given in the Supporting Information.) (B) Calculations corresponding to (A) with the assumption of a heterogeneous biexciton decay. A homogeneous decay would give identical curves. The experiments are consistent with theory, but must be redesigned to extract meaningful new information.

dependence of their results or the relative signs or amplitudes of the components assigned to excitons and biexcitons. However, the results found here show that these factors have little effect on the time constants measured. The biexciton decay is the only new component added, whether saturation occurs or does not.

Expanding our scope to include $\tau_2 > 0$ brings the new biexciton−biexciton correlation function $C_{2'2'}(\tau_2, \tau_1)$ into play (eq 37). The biexciton and exciton have already been shown to be uncorrelated, $C_{2'1'}(\tau_2, \tau_1) = C_{2'}(\tau_2)C_{1'}(\tau_1)$ (part I, section 5), so the two limiting possibilities are that the biexciton dispersion is homogeneous, $C_{2'2'}(\tau_2, \tau_1) = C_{2'}(\tau_2)C_{2'}(\tau_1)$, and

$$A_1^{(2)}(\tau_2, \tau_1) = \frac{1}{2}e^{i\Phi_{12}}C_{2'}(\tau_2)(C_{2'}(\tau_1) + C_{1'}(\tau_1)) \tag{41}$$

or the dispersion is heterogeneous, $C_{2'2'}(\tau_2, \tau_1) = C_{2'}(\tau_2 + \tau_1)$, and

$$A_1^{(2)}(\tau_2, \tau_1) = \frac{1}{2}e^{i\Phi_{12}}(C_{2'}(\tau_2 + \tau_1) + C_{2'}(\tau_2)C_{1'}(\tau_1)) \tag{42}$$

These two cases are only distinguishable when τ_1 is near the biexciton half-life τ_b. If $\tau_1 \ll \tau_b$, then eq 39 holds. On the other hand, if $\tau_1 \gg \tau_b$, then $C_{2'2'}(\tau_2,\tau_1) \approx 0$, and eq 37 reduces to

$$A_1^{(2)}(\tau_2, \tau_1) = \frac{1}{2}e^{i\Phi_{12}}C_{2'1'}(\tau_2, \tau_1); \quad \tau_1 \gg \tau_b \tag{43}$$

Either limit is insensitive to the heterogeneity of the rate dispersion.

Our data are shown in Figure 4A. No change in shape with τ_1 is evident, a result that is consistent with eq 41. However, only the data set with $\tau_1 = 10$ ps is in the sensitive range, and the biexciton−biexciton correlation is diluted by averaging with the biexciton−exciton correlation function (eq 37).

To judge the expected effects, calculations for the data assuming biexciton heterogeneity (eq 42) and the 1D functions measured in part I are shown in Figure 4B. If the biexciton relaxation were homogeneous (eq 41), all the curves in this figure would be identical. With an assumption of heterogeneity, there is a difference, and it is largest for $\tau_1 = 10$ ps, as expected. However, the effect is quite small, and the current data cannot comment on the heterogeneity of the biexciton decay. Although we do not gain any new information from Figure 4, it does further confirm the completeness of the theory.
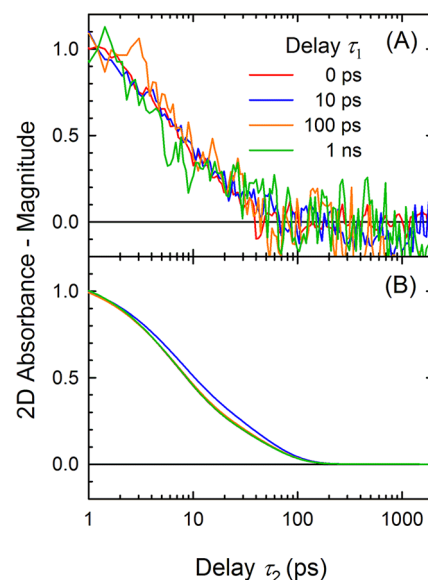
Although this data set is not ideal for measuring biexciton−biexciton heterogeneity, these calculations show how the measurements could be improved. More data should be taken over the range of τ_1 corresponding to the biexciton decay. In addition, the fluence of the second excitation should be kept low, and only the fluence of the first should be increased. In this case, the set of pathways in Figure 2C, which contribute $C_{2'1'}(\tau_2, \tau_1)$ to eq 37, would be eliminated, and only those in Figure 2B, which create $C_{2'2'}(\tau_2, \tau_1)$, would be retained.

3. THERMAL EFFECTS: THEORY

The analysis in part I of the paper ignored any signal from heating of the solvent, but in principle, all of the transient-grating and MUPPETS measurements at long times could be perturbed by thermal effects. Some measurements (e.g., Figure I.9B) appear to have a thermal signal; others are more ambiguous. This section develops the theory, methods, and analysis needed to quantify the thermal effects in all these measurements.

Methods to extend the pathway formalism to thermal signals have been developed for two-level systems[10] and also for excitonic systems.[5] These methods and notation are reviewed in subsection 3.1 to setup the calculations in subsection 3.2, the extension to fluence-induced data in subsection 3.3 and the comparison to data in section 4.

3.1. Including Thermal Signals in Pathways. The calculations are greatly simplified by the linearity of the solvent thermal response. As a result, only heat generated in the final time period is detectable.[10] The generalized absorbance due to thermal effects is calculated from[5]

$$A_\varepsilon^{(N)}(\tau_N, ..., \tau_1) = (-1)^N \rho L[\sigma_\varepsilon | C_\varepsilon(\tau_N)$$
$$\times \mathbf{G}_\varepsilon(\Gamma + t_{N-1}, t_{N-1})\mathbf{T}_N...\mathbf{G}(t_1, t_0)\mathbf{T}_1|eq] \tag{44}$$

and adds to the fully resonant absorbance (eq 2). The solute time evolution between times t_{N-1} (the time of the final excitation) and t_N (the time of the probe) $G(t_N, t_{N-1})$ is replaced by a product of the thermal-response function $C_\varepsilon(\tau_N)$ and the thermal yield $G_\varepsilon(\Gamma + t_{N-1}, t_{N-1})$. The operator $G_\varepsilon(t_1, t_0)$ measures the total amount of heat deposited in the solvent at time t_1 from electronic states populated at time t_0.

The thermal-response function $C_\varepsilon(\tau_N)$ gives the change in index-of-refraction of the solvent at time τ_N due to heat deposited at time zero. It consists of a purely thermal component, which decays slowly on our time scale, and an acoustic component with a period 4Γ. Over short times, it is sufficient to use the simple approximation[10]

$$C_\varepsilon(\tau_N) = 1 - \cos\left(\frac{\tau_N}{4\Gamma}\right) \tag{45}$$

The acoustic period is calculated from the experimental geometry and the speed-of-sound of the solvent. In our system, $\Gamma = 1.27$ ns. Thus the biexciton decay is nearly instantaneous compared to the thermal response, but the exciton decay is not.

Equation 44 makes the approximation that any heat deposition before Γ (half way to the first maximum) is instantaneous and any heat deposited after Γ has no effect. This approximation is reasonable for the CdSe/Zn exciton decay, which has significant components before and after Γ, but only a small decay in the region near Γ. Under this approximation, $G_\varepsilon(\Gamma + t_{N-1}, t_{N-1})$ does not contribute to the time evolution of the signal, and convolutions are avoided.

In eq 44, the states describing the system must be expanded to $|P\ n_\varepsilon]$. The electronic state of the solute is P, as before. The added variable n_ε measures the change in solvent energy as the number of excitation photons of frequency ω that are converted to heat per solute.[5] Because thermal effects are only created over the last time period, the variable n_ε can be suppressed during earlier periods (see, for example, Figures 5 and 6).

The other new element in eq 44 is the thermal-detection vector $[\sigma_\varepsilon]$.[5] It has components

(A) Fluence Independent
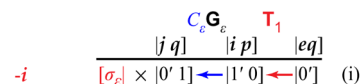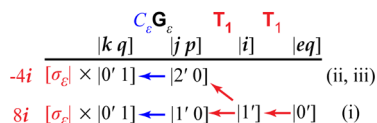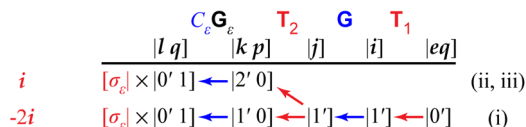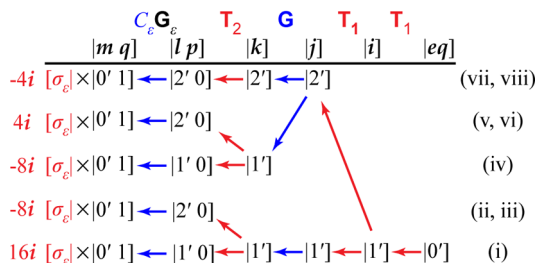
(B) 1st Excitation Saturated

Figure 5. Pathways used to calculate the thermal signal in 1D (pump–probe and transient-grating) experiments, including the fluence dependence. The format is explained in the Figure 1 caption. The time dependence (blue) is governed by the solvent thermal-response operator C_ε. The yield of solvent energy is given by G_ε. The relative weights (left) are shown here for the simple case $\sigma_\varepsilon'' = 1$ and $G_\varepsilon = 1$. The indices on each pathway (right) indicate the corresponding resonant pathways in Figure 1. The later states $|P\ n_\varepsilon]$ are expanded to include the number of photons converted to solvent heat n_ε. (A) Pathways with no fluence dependence. (B) Pathways with fluence dependence due to two interactions with the excitation pulses. (C) Pathways with fluence dependence due to two interactions with the detection pulses.

(A) Fluence Independent

(B) 1st Excitation Saturated
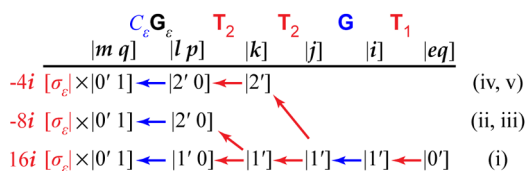
(C) 2nd Excitation Saturated

Figure 6. Pathways used to calculate the thermal signal in 2D (MUPPETS) experiments. The format is explained in the captions to Figures 1 and 5. The indices on each pathway indicate the corresponding resonant pathways in Figure 2. (A) Pathways with no fluence dependence. (B) Pathways with fluence dependence due to two interactions with the excitation pulses. (C) Pathways with fluence dependence due to two interactions with the detection pulses.

$$(\sigma_\varepsilon)^{in_\varepsilon} = i\sqrt{2}\,\sigma_\varepsilon'' \delta_0^i n_\varepsilon \tag{46}$$

where i is the solute electronic state in the exciton basis set. It is purely imaginary, as expected for a nonresonant process. The magnitude of the thermal signal is determined by the thermal cross-section σ_ε'', which is defined by

$$\sigma_\varepsilon'' = \frac{\omega}{c}\left(1 + \frac{1}{n_s^2}\right)\left(\frac{-dn_s}{d\rho}\right)\left(\frac{d\rho_s}{d\varepsilon_s}\right)\hbar\omega \tag{47}$$

where n_s is the solvent index-of-refraction, and ρ_s is the solvent density. Although σ_ε'' is a property of the solvent, it has the units of a cross-section and plays a role analogous to a solute absorption cross-section.

Equation 44 can be expanded into pathways by inserting sets of states between the operators. The result is

$$\frac{A_\varepsilon^{(N)}(\tau_N, ..., \tau_1)}{A'^{(0)}} = (-1)^N I^N [(\sigma_\varepsilon)^{nq}(\sigma_T)_m^l \cdots (\sigma_T)_k^j]$$

$$\times C_\varepsilon(\tau_N)\langle (G_\varepsilon)_{nq}^{mp}(\Gamma + t_{N-1}, t_{N-1})$$

$$\times G_l^k(t_{N-1}, t_{N-2})...G_j^{1'}(t_1, t_0)\rangle \tag{48}$$

(cf. eqs 8 and 9). Where double indices occur, the first refers to the solute electronic state and the second to the solvent energy.

In the exciton basis set, the selection rules on $(G_\varepsilon)_{nq}^{mp}(t_1, t_0)$ are quite restrictive. The only nonzero elements are

$$(G_\varepsilon)_{0'1}^{1'0}(t_1, t_0) = \frac{Q_1}{\sqrt{2}}(1 - G_{1'}^{1'}(t_1, t_0)) \tag{49}$$

and

$$(G_\varepsilon)^{2'0}_{0'1}(t_1, t_0) = \frac{Q_2}{\sqrt{2}}(1 - G_{2'}^{2'}(t_1, t_0)) - \frac{Q_1}{\sqrt{2}}G_{1'}^{2'}(t_1, t_0)$$

$$(50)$$

In our model, we have allowed for the possibility that the exciton or biexciton may decay to a high energy "trap" state, and thus, does not release heat to the solvent. The fraction of the energy released as heat is Q_1 or Q_2 for the exciton or biexciton respectively. The derivation of eqs 49 and 50 is given in the Supporting Information.

3.2. Calculating Low-Fluence Thermal Signals. The sequence of operators that creates the low-fluence, 1D thermal absorbance is

$$A^{(1)}_{\varepsilon A}(\tau_1) = -\rho L[\sigma_\varepsilon | C_\varepsilon(\tau_1)\mathbf{G}_\varepsilon(\Gamma + t_0, t_0)\mathbf{T_l}|eq]$$

$$(51)$$

There is only one allowed pathway (Figure 5A) just as there is only one low-fluence, fully resonant pathway (Figure 1A and eq 10). This pathway gives a contribution to the absorption of

$$\frac{A^{(1)}_{\varepsilon A}(\tau_1)}{A'^{(0)}} = -i\sigma_\varepsilon'' I C_\varepsilon(\tau_1)Q_1(1 - C_{1'}(\Gamma))$$

$$(52)$$

(c.f. eq 17).

The sequence of operators that creates the low-fluence, 2D thermal absorbance is

$$A^{(2)}_{\varepsilon A}(\tau_2, \tau_1) = \rho L[\sigma_\varepsilon | C_\varepsilon(\tau_2)\mathbf{G}_\varepsilon(\Gamma + t_1, t_1)\mathbf{T_2G}(t_1, t_0)\mathbf{T_l}|eq]$$

$$(53)$$

It is expanded to two pathways in Figure 6A, whereas the corresponding fully resonant signal $A^{(2)}_A(\tau_2, \tau_1)$ has three pathways (Figure 2A). However, eq 50 has two terms for the detection of the biexciton state, the first associated with diagonal biexciton decay and the second with cross-relaxation. When the thermal pathways are evaluated, they give three terms:

$$\frac{A^{(2)}_{\varepsilon A}(\tau_2, \tau_1)}{A'^{(0)}} = -i\sigma_\varepsilon'' I^2 C_\varepsilon(\tau_2)[2\sigma'_{01}Q_1(C_{1'}(\tau_1)$$
$$- C_{1'1}(\Gamma, \tau_1)) + \sigma'_{12}Q_1 C_{1'1}^{2'}(\Gamma, \tau_1)$$
$$- \sigma'_{12}Q_2(C_{1'}(\tau_1) - C_{2'1}(\Gamma, \tau_1))]$$

$$(54)$$

An important result of this calculation is that for each resonant pathways in Figure 2A there is a corresponding thermal term in eq 54. During τ_2, the first terms in both eqs 18 and 54 concern exciton dynamics, the second terms involve cross-relaxation, and the last terms deal with biexciton dynamics. The correspondence between resonant and thermal pathways is indicated in Figures 5 and 6 by labeling with the corresponding indices from Figures 1 and 2.

3.3. Calculating Fluence-Induced Thermal Signals. Following the methods of section 2, the calculation of thermal effects can by extended to the first-order, fluence-induced signals. In 1D, the first excitation can have a double interaction, leading to a thermal contribution to the absorbance

$$A^{(1)}_{\varepsilon B}(\tau_1) = -\rho L[\sigma_\varepsilon | C_\varepsilon(\tau_1)\mathbf{G}_\varepsilon(\Gamma + t_0, t_0)\mathbf{T_l T_l}|eq]$$

$$(55)$$

This term expands into two pathways (Figure 5B). Evaluating those pathways leads to three terms in the thermal absorbance

$$\frac{A^{(1)}_{\varepsilon B}(\tau_1)}{A'^{(0)}} = 4i\sigma_\varepsilon'' I^2 C_\varepsilon(\tau_1)[2\sigma'_{01}Q_1(1 - C_{1'}(\Gamma)) + \sigma'_{12}C_{1'}^{2'}(\Gamma)$$
$$- \sigma'_{12}Q_2(1 - C_{2'}(\Gamma))]$$

$$(56)$$

A factor of $\varepsilon_2 = 4$ to account for phase-matching degeneracy is included in eq 56 and in the weights given in Figures 5 and 6. These three terms are in one-to-one correspondence with the corresponding resonant absorbance (eq 23). Because the thermal-grating signal requires time to develop, there is no effect from two interactions with the detection pulses, i.e., no analogue of the pathways in Figure 5C.

A similar approach in 2D generates signals due to double interaction of the first pulse

$$A^{(2)}_{\varepsilon B}(\tau_2, \tau_1) = \rho L[\sigma_\varepsilon | C_\varepsilon(\tau_2)\mathbf{G}_\varepsilon \mathbf{T_2G}(t_1, t_0)\mathbf{T_l T_l}|eq]$$

$$(57)$$

or with the second pulse

$$A^{(2)}_{\varepsilon C}(\tau_2, \tau_1) = \rho L[\sigma_\varepsilon | C_\varepsilon(\tau_2)\mathbf{G}_\varepsilon \mathbf{T_2 T_2 G}(t_1, t_0)\mathbf{T_l}|eq]$$

$$(58)$$

These correspond to the expressions for saturation of the 2D resonant signal $A^{(2)}_B(\tau_2, \tau_1)$ and $A^{(2)}_C(\tau_2, \tau_1)$ (eqs 29 and 30). Expansion of eqs 57 and 58 leads to the pathways shown in Figure 6B and 6C, respectively. The number of terms is large, so we make a detailed evaluation in limits that apply to our system: any term involving cross-relaxation is dropped, and the biexciton relaxation is fast relative to Γ. Evaluating them gives

$$\frac{A^{(2)}_{\varepsilon B}(\tau_2, \tau_1)}{A'^{(0)}} = 4i\sigma_\varepsilon'' I^3 C_\varepsilon(\tau_2)$$
$$\times [(2\sigma'_{01})^2 Q_1(C_{1'}(\tau_1) - C_{1'1}(\Gamma, \tau_1))$$
$$- \sigma'_{12}(2\sigma'_{01})Q_2(C_{1'}(\tau_1) - C_{2'1}(\Gamma, \tau_1))$$
$$- (\sigma'_{12})^2 Q_2(C_{2'}(\tau_1) - C_{2'2}(\Gamma, \tau_1))]$$

$$(59)$$

which is based on pathways i, iii, and viii, and

$$\frac{A^{(2)}_{\varepsilon C}(\tau_2, \tau_1)}{A'^{(0)}} = 4i\sigma_\varepsilon'' I^3 C_\varepsilon(\tau_2)$$
$$\times [(2\sigma'_{01})^2 Q_1(C_{1'}(\tau_1) - C_{1'1}(\Gamma, \tau_1))$$
$$- \sigma'_{12}(2\sigma'_{01})Q_2(C_{1'}(\tau_1) - C_{2'1}(\Gamma, \tau_1))$$
$$- (\sigma'_{12})^2 Q_2(C_{1'}(\tau_1) - C_{2'1}(\Gamma, \tau_1))]$$

$$(60)$$

which is based on pathways i, iii, and v.

4. THERMAL EFFECTS: COMPARISON TO DATA

4.1. Including Thermal Signals in the Fit-Free Analysis. Part I of this paper drew a number of conclusions based on direct comparisons between different sets of data, without any fitting required.[1] In this section, we examine whether including thermal effects changes the validity of those comparisons. The analysis is aided by following the correspondence between fully resonant and thermal terms.

We first consider the comparison of MUPPETS decay slices in τ_2 at different values of τ_1 (Figure I.10). The discussion is simplified by introducing three functions that represent the size of the thermal effects associated with the three resonant MUPPETS pathways:

$$d_{1'1}(\tau_1) = \frac{\sigma_\varepsilon''}{|\sigma_\varepsilon|}Q_1\left(C_{1'}(0) - \frac{C_{1'1}(\Gamma, \tau_1)}{C_{1'}(\tau_1)}\right)$$

$$(61)$$

$$d_{1'1}^{2'}(\tau_1) = \frac{\sigma_\varepsilon''}{|\sigma_e|}Q_1\left(C_{1'}^{2'}(0) - \frac{C_{1'1}^{2'}(\Gamma, \tau_1)}{C_{1'}(\tau_1)}\right) \tag{62}$$

and

$$d_{2'1}(\tau_1) = \frac{\sigma_\varepsilon''}{|\sigma_{12}|}Q_2\left(C_{2'}(0) - \frac{C_{2'1}(\Gamma, \tau_1)}{C_{1'}(\tau_1)}\right) \tag{63}$$

The first function $d_{1'1}(\tau_1)$ is associated with the exciton–exciton pathway (Figures 2A.i and I.2A), the second $d_{1'1}^{2'}(\tau_1)$ is associated with the cross-relaxation (Figures 2A.ii and I.2B), and the third $d_{2'1}(\tau_1)$ is associated with the exciton–biexciton pathway (Figures 2I.iii and I.2C).

After the fully resonant (eq 18) and thermal signals (eq 53) are added, the total is normalized (eq I.3), and the low-fluence component is taken (eq 36), the result is

$$A_0^{(2)}(\tau_2, \tau_1) = (e^{i\Phi_e}C_{1'1}(\tau_2, \tau_1) - id_{2'1}(\tau_1)C_\varepsilon(\tau_2)C_{1'}(\tau_1))$$
$$- \frac{1}{2}\frac{\sigma'_{12}}{\sigma'_{01}}(e^{i\Phi_e}C_{1'1}^{2'}(\tau_2, \tau_1) - id_{1'1}^{2'}(\tau_1)C_\varepsilon(\tau_2)C_{1'}(\tau_1))$$
$$- \frac{1}{2}\frac{|\sigma_{12}|\sigma'_{12}}{|\sigma_e|\sigma'_{01}}(e^{i\Phi_{12}}C_{2'1}(\tau_2, \tau_1) - id_{2'1}(\tau_1)C_\varepsilon(\tau_2)C_{1'}(\tau_1)) \tag{64}$$

Each resonant term (the first term within each set of parentheses) has an associate thermal term (the second term in each set of parentheses) with a similar size and sign. The thermal cross-relaxation $d_{1'1}^{2'}(\tau_1)$ will be small whenever the resonant cross-relaxation $C_{1'1}^{2'}(\tau_2, \tau_1)$ is small (eq 62). (The $C_{1'}^{2'}(0) = 0$ term is only included to show symmetry.) Also, the signs of the exciton–exciton and exciton–biexciton thermal terms, $d_{1'1}(\tau_1)$ and $d_{2'1}(\tau_1)$ respectively, have opposite signs, just as the resonant terms do.

The thermal terms in eq 64 are always separable in τ_1 and τ_2. In general, this result will complicate the interpretation of the MUPPETS data, because in many models (for example, Figure I.11B–D), the resonant terms are not separable. In those cases, detailed modeling of the thermal effects is necessary to correctly interpret the data.

However, in one case, when the exciton decay is homogeneous and the biexciton decay is uncorrelated with the exciton decay (see Figure I.11A), the resonant terms are separable in τ_1 and τ_2, and thus, the total signal is as well. In this case, the slices along τ_2 of the MUPPETS data at different values of τ_1 have identical shapes. Thus Figure I.10 remains a valid, fit-free test for this model, regardless of the size of any thermal effects. The conclusions of part I are unchanged.

Section I.4 showed that important conclusions can be obtained from the $\tau_1 = 0$ cut of the MUPPETS data by itself. To discuss this case, three constants, $d_{1'}$, $d_{1'}^{2'}$ and $d_{2'}$, are defined as the $\tau_1 = 0$ limits of the three functions in eqs 61–63:

$$d_i^j = d_i^j(0) \tag{65}$$

They are also associated with 1D exciton, cross-relaxation, and biexciton pathways (Figure 2A.i–iii, respectively). With these definitions, the $\tau_1 = 0$ slice of the MUPPETS signal (eq 64) becomes

$$A_0^{(2)}(\tau_2, 0) = (e^{i\Phi_e}C_{1'}(\tau_2) - id_{1'}C_\varepsilon(\tau_2))$$
$$- \frac{1}{2}\frac{\sigma'_{12}}{\sigma'_{01}}(e^{i\Phi_e}C_{1'}^{2'}(\tau_2) - id_{1'}^{2'}C_\varepsilon(\tau_2))$$
$$- \frac{1}{2}\frac{|\sigma_{12}|\sigma'_{12}}{|\sigma_e|\sigma'_{01}}(e^{i\Phi_{12}}C_{2'}(\tau_2) - id_{2'}C_\varepsilon(\tau_2)) \tag{66}$$

For comparison, the 1D, low-fluence absorbance is derived from eqs 17, 52, I.2, and 27:

$$A_0^{(1)}(\tau_1) = e^{i\Phi_e}C_{1'}(\tau_1) - id_{1'}C_\varepsilon(\tau_1) \tag{67}$$

In both eqs 66 and 67, the correspondence between resonant and thermal terms is maintained. The low-fluence, 1D signal (eq 67) isolates both the resonant and thermal effects of exciton decay. In the MUPPETS signal (eq 66), the thermal effects of exciton and biexciton decay cancel as the resonant signals do. As a result, the thermal signal is smaller MUPPETS than in 1D measurements.

We next look at the biexciton signal $A_b(\tau)$, which is extracted as the difference between the low-fluence 1D signal and the $\tau_1 = 0$ slice of the MUPPETS data

$$A_b(\tau) = 2\frac{\sigma'_{01}|\sigma_e|}{\sigma'_{12}|\sigma_{12}|}(A_0^{(1)}(\tau) - A_0^{(2)}(\tau, 0)) \tag{68}$$

(cf eq I.14). In section 4.2 of part I, the biexciton signal was interpreted as isolating the biexciton decay from the exciton decay, including the exciton decay of photoproducts. A small cross-relaxation term also contributes (see eq I.15). When thermal effects are included by putting eqs 67 and 66 into eq 68, the correspondence between resonant and thermal terms is maintained:

$$A_b(\tau) = (e^{i\Phi_{12}}C_{2'}(\tau) - id_{2'}C_\varepsilon(\tau))$$
$$+ \frac{|\sigma_{12}|}{|\sigma_e|}(e^{i\Phi_e}C_{1'}^{2'}(\tau) - id_{1'}^{2'}C_\varepsilon(\tau)) \tag{69}$$

Equation 69 extends the interpretation given in part I. The biexciton signal also isolates the component of the thermal signal that is attributable to the biexciton decay $d_{2'}$. The small cross-relaxation term also brings along its small thermal signal $d_{1'}^{2'}$. The exciton thermal effects are eliminated along with its resonant signal.

Part I directly compared the biexciton signal $A_b(\tau)$ to the fluence-induced component of the 1D signal $A_1^{(1)}(\tau)$ (Figure I.9B). How this comparison survives the addition of thermal effects depends on the energy of the probe pulses. If the probe pulses are substantially weaker than the excitation pulses, the pathways in Figure 1C can be neglected. Adding the absorbances due to the remaining pathways (Figures 1A–B and 5A–B), normalizing (eq I.2) and taking the linear, fluence-induced term (eq 27) gives

$$A_1^{(1)}(\tau) = (e^{i\Phi_{12}}C_{2'}(\tau) - id_{2'}C_\varepsilon(\tau))$$
$$+ \frac{|\sigma_{12}|}{|\sigma_e|}(e^{i\Phi_e}C_{1'}^{2'}(\tau) - id_{1'}^{2'}C_\varepsilon(\tau)) \tag{70}$$

The correspondence between resonant and thermal terms still holds. In the absence of photoproducts, $A_b(\tau) = A_1^{(1)}(\tau)$.

However, the experiments in part I were done with the probe–pulse fluence equal to that of the excitation pulses. This condition does not alter the low-fluence signal, even with the thermal signal included (eq 67). However, it adds the pathways

in Figure 1C to the fluence-induced signal. Recalculating eq 70 with these terms included gives

$$A_1^{(1)}(\tau_2) = (e^{i\Phi_{12}}C_{2'}(\tau_2) - id_{2'}C_\varepsilon(\tau_2))$$
$$+ \frac{|\sigma_e|}{|\sigma_{12}|}(e^{i\Phi_e}C_{1'}^{2'}(\tau_2) - id_{1'}^{2'}C_\varepsilon(\tau_2))$$
$$+ \left(e^{i\Phi_{12}}C_{2'}(\tau_2) - i\frac{|\sigma_e|\sigma'_{10}}{|\sigma_{12}|\sigma'_{12}}d_{1'}C_\varepsilon(\tau_2)\right) \tag{71}$$

The last set of terms in parentheses is new. These terms do not change the shapes of either the resonant or thermal signals. However, they do perturb the ratio of resonant- to thermal-signal sizes. Part of the biexciton decay is paired with a thermal effect due to excitons: the strict correspondence between resonant and thermal terms is lost. It is lost because resonant detection is subject to saturation, whereas the nonresonant detection of thermal effects is not.

Fortunately, in our system the time scales of the biexciton decay and the thermal signal are distinct. The direct comparison of $A_b(\tau)$ and $A_1^{(1)}(\tau)$, as in Figure I.9B, is still valid at times before the thermal signal rises (<300 ps). At later times, the sizes of the thermals signals may not be identical. In a well-characterized system, eq 71 allows this effect to be calculated. However, using low energy probe pulses in the 1D measurements would have allowed direct comparison of the two results without calculations.

4.2. Measuring the Thermal Cross-Section. Further analysis of the thermal contributions to the data requires fitting to detailed models. The shape of the thermal response under a wide range of conditions has been discussed previously.[19−21] Here, a simple short-time approximation (eq 45) will be sufficient. The acoustic period, $\Gamma = 5.08$ ns, is known from the speed of sound in toluene[22] and the angle between zero- and first-order diffraction, $\alpha = 2.28°$.[10] However, it is not practical to accurately predict the absolute size of the thermal response in the face of numerous experimental imperfections. Fortunately, the results of section 3 allow calibration of the relative thermal cross-section $\sigma_\varepsilon''/|\sigma_e|$ from the data already used to calibrate the phase of our signals (Figure I.4).

Those data are repeated in Figure 7. It consists of transient-grating results from CdSe/ZnS nanoparticles and azulene, each in toluene, taken on the same day with no changes to the apparatus. In this analysis of the data, the focus is on the magnitudes of the absorbances, $|A_{az}^{(1)}(\tau_1)|$ and $|A_{CdSe}^{(1)}(\tau_1)|$ for azulene and CdSe/ZnS, respectively, rather than on their phases. The data for azulene (blue) has a resonant component only before 10 ps, because of the rapid decay of the excited state.[16,23] After this time, the signal is only due to thermal effects, and the data are described by

$$\frac{|A_{az}^{(1)}(\tau_1)|}{A_{az}'^{(0)}} = I\sigma_\varepsilon'' C_\varepsilon(\tau_1) = TC_\varepsilon(\tau_1) \tag{72}$$

(eq 52 with $Q_1 = 1$ and $C_{1'}(\Gamma) = 0$). Using eq 45 for $C_\varepsilon(\tau_1)$, the thermal amplitude T is fit.

The CdSe/ZnS data before thermal effects (<300 ps) and neglecting cross-relaxation is described by
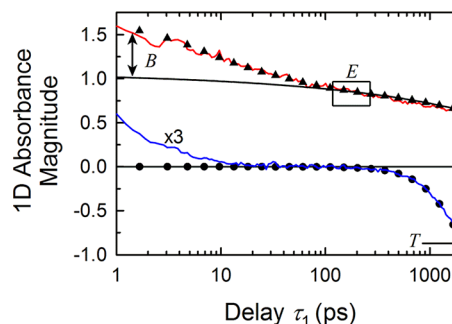

Figure 7. Calibration of the thermal cross-section with an external standard. The magnitude of the transient-grating signal $A^{(1)}(\tau_1)$ of azulene in toluene (blue) and CdSe/ZnS in toluene (red) were measured contemporaneously and with the same excitation energy (10.6 nJ/pulse) (from Figure I.4). The parameters T, E, and B are determined from global fits, but the labels indicate the regions that most clearly determine their values. The fit of late azulene data to eq 72 (black circles) yields the thermal amplitude T. The fit of CdSe/ZnS data to eq 73 (black triangles) yields the exciton amplitude E. The difference between the initial data and $EC_{1'}(\tau_1)$ (black solid curve) yields the biexciton amplitude B. These three fit parameters are sufficient to determine the ratio of thermal and resonant cross sections (eq 74).

$$\frac{|A_{CdSe}^{(1)}(\tau_1)|}{A_{CdSe}'^{(0)}} = |I\sigma_e(1 - 16\sigma'_{12}I)C_{1'}(\tau_1)$$
$$+ 8\sigma_{12}\sigma'_{12}I^2 C_{2'}(\tau_1)|$$
$$= |EC_{1'}(\tau_1) + Be^{i(\Phi_{12}-\Phi_e)}C_{2'}(\tau_1)| \tag{73}$$

(eqs 17, 23, and 26). Because CdSe has a larger absorption cross-section than azulene, we had to use a pulse energy that created some biexcitons in the CdSe sample to get a strong signal from the azulene solution. Thus, eq 73 contains terms for both saturation of the exciton and formation of the biexciton. The data is fit using the forms for $C_{1'}(\tau_1)$ and $C_{2'}(\tau_1)$ found in part I (eqs I.4 and I.5) The exciton magnitude E is well determined by the data near 300 ps, after $C_{2'}(\tau_1)$ has fully decayed and before any potential thermal effects begin. The number of biexcitons is measured by B. It is determined primarily by the increase of the initial signal size over that expected from E. Using eqs 72 and 73, one can solve for the ratio of thermal and exciton cross sections in terms of the fitting parameters

$$\frac{\sigma_\varepsilon''}{|\sigma_e|} = \frac{T}{E}\left[1 + 2\left(\frac{\sigma'_{12}|\sigma_e|}{|\sigma_{12}|\sigma'_{01}}\right)\frac{B}{E}\right]^{-1} = 0.136 \tag{74}$$

This measurement is robust. The pulse energies and various instrumental factors cancel in taking the ratio of the two measurements. Only the static absorbances $A'^{(0)}$ of the two samples are needed to match their properties. Knowledge of the cross sections in the system is only needed to calculate the small deviation from one of the factor in parentheses.

4.3. Modeling Thermal Effects in the Data. A notable result from part I is that good fits to the data were possible without including thermal effects. The absence of thermal effects could imply that the exciton and biexciton decay to relatively high energy trap states without releasing heat. Such a conclusion requires a comparison of the size of predicted effects to the error level of the data. We will show that the thermal signals should exceed the random noise of the experiment, but that systematic errors prevent a firm conclusion.

The absence of a thermal signal is clearest in the fluence-induced transient-grating data $A_1^{(1)}(\tau)$ (Figure 8A). According
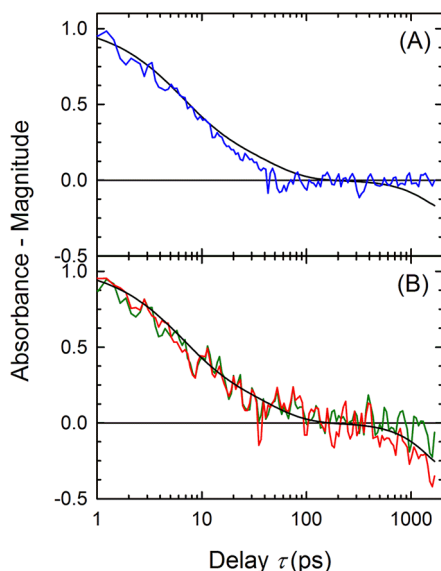

Figure 8. Comparison of the calculated biexciton thermal signal with $Q_2 = 1$ (black) to various measurements. (A) The fluence-induced transient-grating magnitude $|A_1^{(1)}(\tau)|$ (blue, from Figure I.5C) does not show a thermal signal at long times. (B) The biexciton signal derived from MUPPETS measurements changes with the 1D decay used in the calculation. Using transient-grating data (red, same as Figure I.9B) is consistent with a strong thermal signal. Using the pump−probe-based model of part I (green) is not.

to eq 71, the biexciton decay at short time should be accompanied by a long-time signal from the heat released by the biexciton decay. However, the data show no signal at long time. Figure 8A also shows the predicted thermal signal (eq 71) if $Q_2 = 1$, i.e., if all the biexciton energy were released as heat. Although the predicted size is smaller than the resonant signal, it should be visible above the experimental noise. These data imply that $Q_2 \approx 0$.

In contrast, the biexciton signal $A_b(\tau)$, shown previously in Figure I.9B and repeated in Figure 8B (red), does show a pronounced long time signal. Calculations with $Q_2 = 1$ (eq 69) are consistent with its size and shape. (The calculations for $A_b(\tau)$ and $A_1^{(1)}(\tau)$ are different due to probe saturation. This effect is not sufficient to explain the difference between these data sets.)

That biexciton signal was calculated by using the transient-grating data to represent $A_0^{(1)}(\tau)$ in eq 68. It is also possible to use the model for $C_{1'}(\tau)$ defined in section 3.2 of part I. This calculation yields the green data in Figure 8B. In this version of the biexciton signal, the thermal signal is missing, again suggesting $Q_2 \approx 0$.

The difficulty in measuring the heat yield from the biexciton decay Q_2 is mirrored by a difficulty in measuring the heat yield from the exciton decay Q_1. Both problems originate in a discrepancy between the pump−probe and transient-grating data at long times. These two 1D data sets are compared in Figure 9. The pump−probe measurement should be the real part of the complex transient-grating signal. The pump−probe data and the transient-grating magnitude are the same at early times, and the transient-grating phase is constant. These early data are consistent with each other. At long times, the pump−
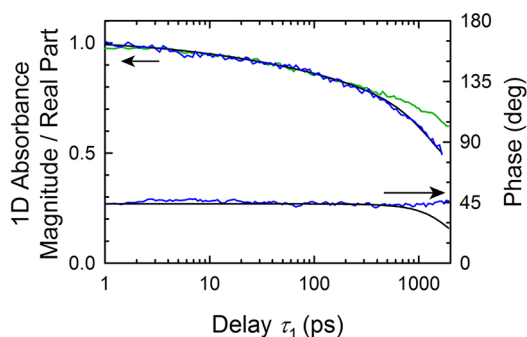

Figure 9. Comparison of low-fluence 1D measurements: real pump−probe (green, from Figure I.6B) and complex transient-grating (blue, from Figure I.5C−D) data. The transient-grating magnitude can be accounted for by adding an imaginary, thermal component to the pump−probe results (black curves), but in that case, the phase of the transient-grating should not be constant.

probe data and the transient-grating magnitude diverge. This difference could be accounted for by including an imaginary thermal signal, which would only affect the transient-grating data. A calculation using the pump−probe fit (eq I.4) for $C_{1'}(\tau_1)$ and $Q_1 = 1$ for the thermal effect (eq 67) is shown, and it matches the transient-grating magnitude quite well. Unfortunately, the thermal-grating phase is constant at long times, which is inconsistent with a significant, imaginary thermal contribution, as shown in Figure 9. Thus, the transient-grating phase implies $Q_1 = 0$, whereas the comparison of pump−probe and transient-grating magnitudes suggest $Q_1 = 1$. The ambiguity in the 1D data also translates into the calculation of the biexciton signal (Figure 8) and thus into determining the thermal yield from the biexciton Q_2.

The last set of data to consider is the MUPPETS data by itself. As argued above, the qualitative interpretation of the MUPPETS data (e.g., Figure I.10) is independent of the size of the thermal contribution. However, quantitative modeling depends on the 1D response, including its thermal component. In part I, a hybrid model was used to fit the MUPPETS data: the magnitude of $C_{1'}(\tau_1)$ was taken from the pump−probe fit, but the phase was taken as a constant, as given by the transient-grating experiments. The constant-phase assumption correctly accounts for the MUPEPTS phase and magnitude (Figure I.11). The lack of a thermal contribution to the MUPPETS phase means that $2Q_1 = Q_2$ and implies that $Q_1 < 0.5$, at least.

It is also possible to model the MUPPETS data using $Q_2 = 1$ along with the model in Figure 9 that reconciles the pump−probe and transient-grating magnitude ($Q_1 = 1$). The magnitude of the MUPPETS data can be fit correctly this way, but the predicted phase is no longer correct (not shown), as with the 1D data in Figure 9.

In conclusion, the discrepancy between pump−probe and transient-grating data is not large enough to affect any of the conclusions about the exciton and biexciton conclusion in part I. However, they create enough uncertainty to prevent a conclusion regarding the role of trap states in the decay.

The inconsistency between pump−probe and transient-grating measurements persisted despite repeated measurements of both. It must be attributed to an unresolved instrumental error. We point out that this problem would not be noticed without a complete measurement of both pump−probe and phase-resolved transient-grating data with calibrated, absolute

phases. These measurement may appear to be redundant, but their comparison is an important control for systematic errors.

5. SUMMARY

This paper has looked at secondary processes that have the potential to interfere with the interpretation of MUPPETS experiments, specifically saturation and solvent heating. It serves three different ends: it derives the theory needed to calculate these effects, it shows that these effects do not alter the conclusions of part I of the paper,[1] and it provides a specific example of these effects to aid in designing and analyzing future experiments.

The incoherent-pathway formalism[2,3] has been extended to allow a systematic calculation of fluence-induced effects, thermal effects and even fluence-induced thermal effects in MUPPETS experiments. Although these processes are well understood in 1D experiments, the methods presented here provide a convenient method for calculating them. It is particularly useful in heterodyned experiments on multilevel systems, where multiple transitions with different phases must be considered.

In contrast, the calculation of fluence-induced effects in MUPPETS is new. The change in sign of the biexciton signal with increasing fluence was satisfactorily explained. The ability to quantitatively model this $\chi^{(7)}$ experiment increases our confidence that our model for CdSe is complete and that no unexpected species, such as triexcitons or photoproducts, occur under our conditions. In general, understanding fluence-induced effects is important in high order spectroscopies such as MUPPETS, as high fluences are often needed to obtain sufficient signal size.

A new correlation function $C_{2'2'}(\tau_2, \tau_1)$, which has information on the heterogeneity of the biexciton decay, is accessible, in principle, by deliberately creating and measuring a fluence-induced signal. Although the current data set addresses this point poorly, the theory suggests methods for improving the experimental design to address this quantity.

In the calculations, processes detected through solvent heating were placed on the same footing as resonantly detected processes. This approach led to a robust method of predicting the size of thermal signals using an external standard. In principle, this method can lead to the identification of spectroscopically dark, trap states. The low ratio of thermal to resonant cross sections in this system along with small inconsistencies in the 1D data undermined this approach here. However, the obstacles that must be overcome are now well-defined.

Overall, none of the interpretations of part I are altered by these effects. For example, the comparison of 1D and MUPPETS data to separate exciton and biexciton dynamics is still valid, if we understand these dynamics to include the thermal effects attributable to relaxation across each transition. However, in many cases thermal effects were unimportant only because of specific features of the nanoparticle system studied. For example, the MUPPETS modeling is unaffected by thermal effects only because there is no evidence for exciton heterogeneity or exciton–biexciton correlation. More generally, modeling of thermal effects is important for the quantitative interpretation of MUPPETS results. This paper makes that modeling possible.

■ ASSOCIATED CONTENT

ⓢ Supporting Information

Derivation of the model for $(G_\varepsilon)^{mp}_{nq}(t_1, t_0)$ given in eqs 49 and 50 and phases for the data in Figure 4A. This information is available free of charge via the Internet at http://pubs.acs.org.

■ AUTHOR INFORMATION

Corresponding Author

*E-mail: berg@sc.edu.

Present Address

[†]Department of Chemistry, Indian Institute of Technology, Guwahati, 781039, Assam, India

Notes

The authors declare no competing financial interest.

■ REFERENCES

(1) Sahu, K.; Wu, H.; Berg, M. A. Multiple Population-Period Transient Spectroscopy (MUPPETS) of CdSe/ZnS Nanoparticles. I. Exciton and Biexciton Dynamics. *J. Phys. Chem. B* **2013**, DOI: 10.1021/jp405785a.

(2) Berg, M. A. Hilbert-Space Treatment of Incoherent, Time-Resolved Spectroscopy. I. Formalism, a Tensorial Classification of High-Order Orientational Gratings and Generalized MUPPETS "Echoes". *J. Chem. Phys.* **2010**, *132*, 144105.

(3) Berg, M. A. Hilbert-Space Treatment of Incoherent, Time-Resolved Spectroscopy. II. Pathway Description of Optical Multiple Population-Period Transient Spectroscopy. *J. Chem. Phys.* **2010**, *132*, 144106.

(4) Berg, M. A. Multidimensional Incoherent Time-Resolved Spectroscopy and Complex Kinetics. *Adv. Chem. Phys.* **2012**, *150*, 1−102.

(5) Wu, H.; Berg, M. A. Multiple Population-Period Transient Spectroscopy (MUPPETS) in Excitonic Systems. *J. Chem. Phys.* **2013**, *138*, 034201.

(6) Eichler, H.; Stahl, H. Time and Frequency Behavior of Sound Waves Thermally Induced by Modulated Laser Pulses. *J. Appl. Phys.* **1973**, *44*, 3429−3435.

(7) Miller, R. J. D.; Casalegno, R.; Nelson, K. A.; Fayer, M. D. Laser-Induced Ultrasonics: A Dynamic Holographic Approach to the Measurement of Weak Absorptions, Optoelastic Constants and Acoustic Attenuation. *Chem. Phys.* **1982**, *72*, 371−379.

(8) Nelson, K. A.; Miller, R. J. D.; Lutz, D. R.; Fayer, M. D. Optical Generation of Tunable Ultrasonic Waves. *J. Appl. Phys.* **1982**, *53*, 1144−1149.

(9) Nelson, K. A.; Fayer, M. D. Laser Induced Phonons: A Probe of Intermolecular Interactions in Molecular Solids. *J. Chem. Phys.* **1980**, *72*, 5202−5218.

(10) Sahu, K.; Berg, M. A. Thermal Gratings and Phase in High-Order, Transient-Grating Spectroscopy. *J. Chem. Phys.* **2011**, *134*, 144502.

(11) Sahu, K.; Kern, S. J.; Berg, M. A. Heterogeneous Reaction Rates in an Ionic Liquid: Quantitative Results from 2D-MUPPETS. *J. Phys. Chem. A* **2011**, *115*, 7984−7993.

(12) Andrews, J. R.; Hochstrasser, R. M. Transient Grating Studies of Energy Deposition in Radiationless Processes. *Chem. Phys. Lett.* **1980**, *76*, 207−212.

(13) Genberg, L.; Bao, Q.; Gracewski, S.; Miller, R. J. D. Picosecond Transient Thermal Phase Grating Spectroscopy: A New Approach to the Study of Vibrational Energy Relaxation Processes in Proteins. *Chem. Phys.* **1989**, *131*, 81−97.

(14) Morais, J.; Ma, J.; Zimmt, M. B. Solvent Dependence of the Twisted Excited State Energy of Tetraphenylethylene: Evidence for a

Zwitterionic State from Picosecond Optical Calorimetry. *J. Phys. Chem.* **1991**, *95*, 3885−3888.

(15) Terazima, M. Reaction Enthalpy and Reaction Volume Changes Upon Photoenolization: 2-Methylbenzophenone. *J. Phys. Chem. A* **1998**, *102*, 545−551.

(16) Kimura, Y.; Fukuda, M.; Kajimoto, O.; Terazima, M. Study on the Vibrational Energy Relaxation of *p*-Nitroaniline, *N,N*-Dimethyl-*p*-nitroaniline, and Azulene by the Transient Grating Method. *J. Chem. Phys.* **2006**, *125*, 194516.

(17) Lebedev, L. P.; Cloud, M. J. *Tensor Analysis*; World Scientific Publishing: Singapore, 2003.

(18) Huxter, V. M.; Scholes, G. D. Nonlinear Optical Approach to Multiexciton Relaxation Dynamics in Quantum Dots. *J. Chem. Phys.* **2006**, *125*, 144716.

(19) Yan, Y.-X.; Cheng, L.-T.; Nelson, K. A. The Temperature-Dependent Distribution of Relaxation Times in Glycerol: Time-Domain Light Scattering Study of Acoustic and Mountain-Mode Behavior in the 20 MHz−3 GHz Frequency Range. *J. Chem. Phys.* **1988**, *88*, 6477−6486.

(20) Sun, T.; Morais, J.; Diebold, G. J.; Zimmt, M. B. Investigation of Viscosity and Heat Conduction Effects on the Evolution of a Transient Picosecond Photoacoustic Grating. *J. Chem. Phys.* **1992**, *97*, 9324−9334.

(21) Fukuda, M.; Kajimoto, O.; Terazima, M.; Kimura, Y. Application of the Transient Grating Method to the Investigation of the Photo-Thermalization Process of Malachite Green in Room Temperature Ionic Liquids. *J. Mol. Liq.* **2007**, *134*, 49−54.

(22) George, J.; Sastry, N. V. Densities, Excess Molar Volumes, Viscosities, Speeds of Sound, Excess Isentropic Compressibilities, and Relative Permittivities for $C_mH_{2m+1}(OCH_2CH_2)_nOH$ (*m* = 1 or 2 or 4 and *n* = 1) + Benzene, + Toluene, + (*o*-, *m*-, and *p*-) Xylenes, + Ethylbenzene, and + Cyclohexane. *J. Chem. Eng. Data* **2003**, *48*, 977−989.

(23) Kimura, Y.; Yamamoto, Y.; Terazima, M. Vibrational Energy Relaxation of Azulene Studied by the Transient Grating Method. II. Liquid Solvents. *J. Chem. Phys.* **2005**, *123*, 054513.

15284

dx.doi.org/10.1021/jp4057913 | *J. Phys. Chem. B* 2013, 117, 15272−15284